Hydrodynamical models of aspherical planetary nebulae

Mellema, G.; Eulderink, F.; Icke, V.

Astron. Astrophys. 252, 718–732 (1991)

ASTRONOMY AND ASTROPHYSICS

Hydrodynamical models of aspherical planetary nebulae

G. Mellema, F. Eulderink*, and V. Icke

Sterrewacht Leiden, P.O.Box 9513, NL-2300 RA Leiden, The Netherlands

Received September 15, 1990; accepted August 8, 1991

Abstract. We present the results of numerical hydrodynamical simulations of the emergence of aspherical planetary nebulae. The computations were done using the 'Roe-solver' method, a characteristic based method never before used in astrophysics. It is briefly described in the article.

Our results show that a wide range of morphologies can be formed by assuming that intermediate-mass stars, in the terminal phases of their evolution, lose mass in at least two successive hydrodynamical stages. During the first stage, which presumably takes place while the star is on the asymptotic giant branch, the stellar wind is slow, dense, and aspherical. The second stage consists of a fast, tenuous, spherical wind which collides with the remains of the preceding slow wind. The interaction between these two winds produces a pattern of hydrodynamic events which gives rise to nebular shapes that can be identified with observed morphologies. The elliptical and 'butterfly' type nebulae form as a consequence of different density distributions in the slow wind. The butterfly type shows a high degree of collimation inside the bubble, resembling jet-like structures. This constitutes a novel collimation mechanism, which may have applications beyond planetary nebulae.

Apart from some minor differences, our results confirm the analytical ones of Icke (1988) and the numerical ones of Icke et al. (1991).

Key words: Planetary Nebulae: general – Hydrodynamics – Numerical Methods – Interstellar Medium: bubbles

1. Introduction

It is now a generally accepted idea that a planetary nebula (PN) is formed from the gas lost by a low– to intermediate mass star, during the Asymptotic Giant Branch (AGB)-phase. This old idea (going back to Shklovskii 1956) has gained considerable interest since the IRAS mission, which made it possible to study the stars at the tip of the AGB and the stars in transition from the AGB to the PN phase. These stars only show up in the infrared because the dusty gas surrounding them inhibits optical detection. Work of e.g. Habing et al. (1989), shows that the late AGB stars (such as OH/IR stars) are indeed the most likely progenitors of PN stars. As the material surrounding them moves out, and the mass loss stops, a PN may form.

One of the more successful scenarios for the formation of spherical PNe from this AGB-wind remnant is the interacting winds model, also known as the two-wind model, which, based on the work of Castor et al. (1975) and Weaver et al. (1977), was proposed by Kwok et al. (1978). According to this model, a PN forms through the interaction of a fast wind, originating from the central star, with the AGB-wind remnant (or slow wind). The fast wind has been observed in many central stars (see Perinotto 1989 for a review) and the halo or shell (often seen around the actual nebula) may be identified with the remnant of the AGB-wind (Frank et al. 1991).

Since Renzini (1981), it is customary to differentiate between two mass loss phases on the AGB. They both have about the same outflow velocity ($\approx$ 10 km s^{-1}), but differ in mass loss rates. The first phase, called the old wind or just AGB wind, is the mass loss observed in Miras, with a typical mass loss rate of $\dot{M} = 10^{-7}$–10^{-6} M$_\odot$ yr^{-1}. The second phase is identified with the mass loss from OH/IR stars, and is called the super wind. It has $\dot{M} = 10^{-5}$–10^{-4} M$_\odot$ yr^{-1}. Models taking into account the interaction between these two slow winds and the fast wind, are called 'three wind models'.

The fast wind has a typical velocity of about 2000 km s^{-1} and quickly overtakes the slow wind. The interaction results in a shock moving into the slow wind, a contact discontinuity following it, and an inner shock closer to the star (see Castor et al. 1975; Lamers 1983). In this scenario the high density shell between the outward-facing shock and the contact discontinuity shows up as the actual nebula when it is photoionised by the central star. This model can explain typical PN properties such as the expansion velocities, the observed densities, and the sharp outer rim quite nicely (Kwok 1982; Kahn 1983; Kahn and West 1985).

There have also been some numerical studies into the interacting winds mechanism. Two of them, Okorov et al. (1985) and Schmidt–Voigt & Köppen (1987) take a few of the complicating factors of PN formation into account. These are the heating and cooling and the effect of an evolving star. Although both one–dimensional studies, the extended treatment of these effects had to be combined with a rather crude numerical hydrodynamics code. This need not necessary be a drawback, but in the case of the interacting wind scheme it is (for reasons that will be given below). Figure 8 of Okorov et al. shows the density profile they obtain for the interaction and none of the bubble characteristics (outer shock, contact discontinuity, inner shock) can be discerned, a fact also noticed by the authors themselves. The results of Schmidt–Voigt & Köppen for the interaction can be found in their Fig.6. These results do show the outer and

Send offprint requests to: G. Mellema

* Koninklijke Shell Laboratorium, P.O.Box 3003, NL-1003 AA Amsterdam, The Netherlands

inner shock, but the contact discontinuity can barely be found at the early stages and has diffused away completely at the later ones. The fact that these authors do not resolve the full hydrodynamic structure invalidates much of their conclusions about the dynamical effect of the fast wind. Bedogni & D'Ercole (1989) add much less micro–physics to their hydrodynamics, but do succeed in resolving the three discontinuities. They conclude that the interacting winds model works, but only for a very strict range of outflow velocities and mass loss rates: The ratio of $\dot{M}v$ of fast wind over slow wind should be larger than one. We find no evidence for such a condition (see Sec.6).

The interacting winds model offers a nice explanation for the asphericity of many PNe. As Balick (1987) pointed out, one can obtain many of the different observed morphologies by assuming a density contrast in the AGB-wind remnant. Because of the observed axial symmetry of many PNe, the density distribution is taken to be axisymmetric with higher densities in the equatorial plane and lower densities in the direction of the polar axis. Balick proposes a morphological scheme in which the form of PNe varies from round (R) through elliptical (E) to butterfly (B) shapes, and he explains this sequence as one of increasing density ratio between pole and equator. Balick, Preston, and Icke (1987) further developed this model and proposed a shock focusing mechanism to produce the *ansae*, blobs of low-ionisation material often found along the symmetry axis of PNe.

In order to further explore Balick's hypothesis, one has to do the detailed hydrodynamical calculations implied by the interacting-winds picture. Icke (1988) (henceforth I 88) analytically derived the form of the outer shock for the interaction between a spherical fast wind and an aspherical AGB-wind. The morphologies found indeed resemble the ones observed quite closely, even in extreme cases (Icke & Preston 1989).

To get more realistic models one has to use numerical methods. For the problem at hand one needs a particularly accurate code, since it must deal with very extreme conditions. If one adopts an AGB mass loss of $\sim 10^{-5}$ $M_\odot$ yr^{-1} and a velocity of 10 km s^{-1}, and a fast wind mass loss of $\sim 10^{-8}$ $M_\odot$ yr^{-1} with a velocity of 2000 km s^{-1}, one has a velocity ratio of 200 and a density ratio of 200 000 between the two winds. These contrasts are clearly extraordinary; such extremes are, in part, what makes astrophysical hydrodynamics so very different from the laboratory variety. Accordingly, one's physical intuition about laboratory flows, and their numerical treatment, may not be carried over to the case of interacting-winds PNe without a thorough appraisal of the consequences of discontinuities in velocity, density, and Mach number, where the jumps can exceed three powers of ten.

No first order code can be expected to handle these jumps properly, because even a tiny bit of numerical diffusion will erroneously transport so much gas from the high density region to the low density region, that the density in this low density area will be dominated by it (see Icke 1991 for a further discussion of numerical accuracy).

Thus far two attempts have been made to model aspherical PNe using two–dimensional hydrodynamics. Igumenshchev et al. (1988) used an aspherical super wind, but no fast wind. The super wind phase is followed by a wind phase characterised by a three orders of magnitude lower value of $\dot{M}$ and the same velocity. Their figures are hard to interpret but they do obtain aspherical nebulae. Because of the absence of a fast wind however, the shells are very extended. Soker & Livio (1989) do consider the interaction of a fast wind with an aspherical AGB (super) wind. Their results start promising but unfortunately their PIC method is not capable of treating the contact discontinuity properly and their results for the later stages suffer from a large amount of numerical diffusion.

Icke, Balick and Frank (1991) (henceforth IBF 91), use a Flux Corrected Transport (FCT) method to do the interacting winds problem. We decided to use the time dependent, explicit, second order accurate method described by Roe (1981, 1986), and much extended by the work of Eulderink (1990). It is a characteristic-based scheme, which ensures the accurate treatment of discontinuities, which dominate the problem. Results obtained by Eulderink (1990) for relativistic problems show that the scheme handles extreme problems very well.

This two-front approach to the problem offers the rather unique opportunity to compare numerical hydrodynamical results. The FCT method differs radically from our 'Roe-solver' and the degree to which the computations agree should give a good indication of the reliability of the results.

In this paper we show the results we obtained using our method. The models are adiabatic; no radiation effects are included, because getting the hydrodynamics right first, is a sound base for later, more elaborate models. In Sec.2 we describe the equations and principles of the method. Section 3 contains a discussion of the initial and boundary conditions used. Results are described and discussed in Sec.4. The conclusions are summed up in Sec.5.

2. Equations and Numerical Method

In this paragraph we describe the numerical method that was used to integrate the partial differential equations that govern Eulerian (meaning no viscosity or heat conduction) flow in spherical coordinates (r, θ, ϕ). Because this method has never before been applied to an astrophysical problem, and has not been described before in the astronomical literature, we give a more elaborate description. The treatment will concentrate on the use of spherical coordinates, but the method can be applied to general coordinate systems. It is in fact the nonrelativistic limit of a general relativistic method, which is to be published separately (Eulderink 1990). The subgrid model (Sec.2.3) deserves special attention, since it is new in the computational physics literature, and may be applicable to other numerical hydro methods. We know of one good example (a code of the Flux Corrected Transport type; Boris & Book 1973, 1976), in which the application of this formalism proved to be very useful (Icke 1991).

2.1. Equations

Because of computational limitations and the symmetric appearance of many PNe, cylindrical symmetry is assumed in the flow pattern to be studied. Therefore all flow quantities are independent of the azimuthal angle (ϕ). In addition, the azimuthal velocity that must be present to some degree in real planetary nebulae, is neglected. Thus, from a symmetry point of view, cylindrical coordinates and spherical coordinates are appropriate. We decided to use spherical coordinates for three reasons. First, deviations of the flow pattern from spherical symmetry which arise because of the tangential component of the density gradient in the slow wind, are the most important features of the flow pattern. By choosing spherical coordinates one assures that deviations from radial flow are not induced by the grid. Second, the hot wind starts as a tiny bubble of small radius. To represent such a

bubble by a few cells on a cylindrical grid would produce a very jagged inner boundary condition for the calculations. Third, we will include radiation from the central star in a later version of the models. The effects of this radiation on the flow are easier to calculate in spherical coordinates.

The fluid at a particular point in spacetime can be described by the dependent variables ρ, v_r, v_θ, p, where ρ is the density of the fluid, v_r its radial velocity, v_θ its polar angular velocity, and p the pressure. The Euler equations in spherical coordinates can then be written as

$$W_t + F_r + G_\theta = S, \tag{1}$$

where the index t denotes partial derivation with respect to time, indices r and θ indicate partial derivation along the radial and transverse coordinate directions, and W is a vector in four-dimensional state space:

$$W \equiv r^2 \sin\theta(\rho, \rho v_r, \rho v_\theta, e), \tag{2}$$

F is the radial flux

$$F \equiv r^2 \sin\theta(\rho v_r, \rho v_r^2 + p, \rho v_r v_\theta, (e+p)v_r), \tag{3}$$

G is the polar flux

$$G \equiv r^2 \sin\theta(\rho v_\theta, \rho v_r v_\theta, \rho v_\theta^2 + p/r^2, (e+p)v_\theta), \tag{4}$$

and S is the source term

$$S \equiv r^2 \sin\theta(0, 2p/r + r\rho v_\theta^2, \frac{p\cos\theta}{r^2\sin\theta} - 2\rho v_r v_\theta/r, 0). \tag{5}$$

This form is chosen because it has *no derivatives* of dependent variables in the source term. The advantage of such a formulation is that the source term remains finite everywhere even if discontinuities are present in the flow. An ideal gas is assumed, so the energy density of the fluid is given by $e \equiv \frac{1}{2}\rho(v_r^2 + r^2 v_\theta^2) + p/(\gamma - 1)$, where the gas pressure $p = \rho kT/m_p$. The value of γ is taken to be 5/3.

We now turn our attention to the numerical method that was used to solve the equations above. First it is explained in general terms. To begin with, the region of interest to the flow is covered with a grid of numerical cells. We use an equidistant grid and adopt the usual notation: $A_{i,j}^n$ means quantity A at time $n\Delta t$ at $r = r_0 + i\Delta r$ and at $\theta = \theta_0 + j\Delta\theta$. The precise values of r_0 and θ_0 are given in Sec.3.

In order to have a chance to uncover at least the most fundamental properties of the flow pattern in PNe one has to use a numerical code that has minimal dissipation (to minimise mass diffusion over the contact discontinuity with a typical density contrast of a factor 10^5, for example). Furthermore, the method must be able to treat the strong shocks which appear. Because of these considerations a conservative (finite volume) approach in combination with a Riemann-solver seems appropriate. In this context, "conservative" means that conserved quantities of the equations (total mass and energy) are indeed conserved by the numerical method: what goes into one cell must come out of another. By integrating the numerical equations over the finite volume of a grid cell one has, to second order,

$$\begin{aligned}
&\frac{1}{\Delta t\Delta r\Delta\theta}\int \mathrm{d}r \int \mathrm{d}\theta \left(W^{n+1} - W^n\right) \\
&\quad + \frac{1}{\Delta t\Delta r\Delta\theta}\int \mathrm{d}t \int \mathrm{d}\theta \left(F_{i+\frac{1}{2}} - F_{i-\frac{1}{2}}\right) \\
&\quad + \frac{1}{\Delta t\Delta r\Delta\theta}\int \mathrm{d}t \int \mathrm{d}r \left(G_{j+\frac{1}{2}} - G_{j-\frac{1}{2}}\right) \\
&\quad - \frac{1}{\Delta t\Delta r\Delta\theta}\int \mathrm{d}t \int \mathrm{d}r \int \mathrm{d}\theta S \approx \\
&\frac{1}{\Delta t}\left(\langle W\rangle_{i,j}^{n+1} - \langle W\rangle_{i,j}^n\right) + \frac{1}{\Delta r}\left(F_{i+\frac{1}{2},j}^{n+\frac{1}{2}} - F_{i-\frac{1}{2},j}^{n+\frac{1}{2}}\right) \\
&\quad + \frac{1}{\Delta\theta}\left(G_{i,j+\frac{1}{2}}^{n+\frac{1}{2}} - G_{i,j-\frac{1}{2}}^{n+\frac{1}{2}}\right) - S_{i,j}^{n+\frac{1}{2}} = 0,
\end{aligned} \tag{6}$$

where $\langle W\rangle_{i,j}^n$ is the *average* state at $t = n\Delta t$ in the cell that has its centre at $r = r_0 + i\Delta r$ and $\theta = \theta_0 + j\Delta\theta$. What remains to be done is to find an approximation for the interface fluxes, $F_{i+\frac{1}{2},j}^{n+\frac{1}{2}}$ and $G_{i,j+\frac{1}{2}}^{n+\frac{1}{2}}$, and for the source term at the cell centre, $S_{i,j}^{n+\frac{1}{2}}$, all at the time which is midway between time n and $n+1$, given the average state of a cell at the present time ($\langle W\rangle_{i,j}^n$).

The interface fluxes can be found from the state *at the interface* using a Riemann-solver. Motivated by the excellent performance of Roe's *approximate* Riemann-solver on Cartesian one-dimensional shock tube tests (Chang & Liou 1988), this method was generalised for use in arbitrary coordinates (Eulderink 1990). This generalised method (the actual Roe-solver) was adopted here to find the required quantities at the intermediate time.

Since a Riemann-solver uses the state at the interface as input, we need a prescription how to find the state at the interface from the average state at the cell centre. This prescription is called the *subgrid model*. Furthermore, since the Riemann-solver is intrinsically one dimensional, we need a formalism to split the two-dimensional set of equations, obtaining two sets of equations in one spatial dimension each. This is done using a standard technique known as *flux splitting* or time splitting (Strang 1968). We now look at all of these ingredients (flux splitting, subgrid model, and Roe's approximate Riemann-solver) separately.

2.2. *Flux splitting*

The equations in two space dimensions (2.1) are approximated by one dimensional equations through flux splitting. First, a new state after a half time step is determined by integrating

$$W_t + F_r = R \tag{7}$$

over half a time step. Then, based on this new state,

$$W_t + G_\theta = T \tag{8}$$

is integrated over a full time step to yield a new state, and finally

$$W_t + F_r = R \tag{9}$$

is integrated over half a time step again to yield the final update of the state to $t = (n+1)\Delta t$.

In principle R and T may be chosen arbitrarily, subject to the constraint $R + T = S$. In the following, we will adopt and explain a special choice for these terms.

If the state at the new time is only needed to proceed with the integration, the third step may be combined with the first one of the next integration to yield a single integration over a full time step. It is also useful to switch the sequence. The flux splitting scheme then consists of a first integration over a half time step in the radial direction, followed by full time steps in the polar and radial direction, followed by full time steps in the radial and polar direction, etc. We adopt this last version (cf. Strang 1968).

2.3. Subgrid Model

The subgrid model is the prescription of the flow within one cell, thereby ignoring the interaction of this flow with the flow in neighbouring cells. This is the non-dynamical part of the method. We use it to obtain the state at the interface, where consequently the interaction is solved using Roe's approximate Riemann-solver (Sec.2.4).

Although a subgrid model is used in Cartesian hydrodynamics as well, it usually receives little or no attention there because of triviality: the state within one cell is just assumed to be constant. The Euler equations are more difficult to solve numerically in spherical coordinates than in cartesian coordinates because of at least four reasons:

i) Cells that are equally spaced in r and θ do not have an equal volume.
ii) At the centre and at the polar axis, spherical coordinates have singularities.
iii) Source terms are present, due to the centrifugal and Coriolis pseudo-forces.
iv) A constant state does not guarantee a constant flux.

Difficulties i) and ii) involve the propagation of errors. A flux error which is small compared to the total content of the cell from which it leaves, may not be small compared to the content of a smaller cell into which it transports. The singularities force certain terms to disappear in reality, which may not automatically disappear numerically.

To elucidate points iii) and iv) we consider stationary solutions to the flow equations. Recognizing such solutions is extremely important for dynamical flow simulations, because otherwise numerical evolution is found in a region where no physical evolution occurs, which would immediately falsify the implicit assumption in a hydrocode that physical evolution is dominant over numerical evolution.

Point iv) means that assuming a constant state within each cell, as is common practice in Cartesian hydrodynamics, will result in an interface flux which differs from place to place in that cell. Thus even if the source term is absent, a stationary solution will not be recognised by such a subgrid model. Alternatively one may assume a stationary solution within each cell. If the source term is absent, a stationary solution is simply given by a constant flux. However, this subgrid model does not automatically reproduce the correct average of the state vector over the cell, whereas the first option does. When a source term is in fact present, stationary solutions do not have a constant flux: when $\partial W/\partial t \neq 0$, the gradient of the flux must equal the source term:

$$F_r = R. \tag{10}$$

This is a nontrivial ordinary differential equation which must be solved within each cell. To complicate things even further, the condition to pick the right solution from the family of solutions is given as an *average over the cell* rather than as a condition at a fixed point. This means that the differential equation should be solved several times to iterate to a solution that yields the right integral. Apart from being expensive, this solution may not even be unique: sub– and supersonic branches will generally occur, and dealing with these is costly, in particular when the cell contains a sonic point. Therefore, in practice one is forced to renounce either the differential equation, and with it the recognition of stationary solutions, or the integral condition. In view of the importance of correctly reproducing stationary solutions, the latter option is chosen. Rather than using the integral condition, the flux is fixed by assuming that the state at the cell centre is given by the known value of the cell-averaged state. But even then one still has to integrate the ordinary differential equation. This may be done analytically provided that the source term is split appropriately (Eulderink 1990):

$$R = r\sin\theta(0, 2p + r^2\rho v_\theta^2, -2\rho v_r v_\theta, 0) \tag{11}$$

$$T = (0, 0, p\cos\theta, 0). \tag{12}$$

For this analytical solution an implicit relation has to be solved iteratively. To evade this expensive method, we use the same source term splitting, but integrate using a one-step numerical approximation, starting from the cell centres to the left and to the right of the cell wall where we want to know F:

$$F_L^n = F_{i,j}^n + \frac{1}{2}\Delta r R_{i,j}^n, \tag{13}$$

$$F_R^n = F_{i+1,j}^n - \frac{1}{2}\Delta r R_{i+1,j}^n, \tag{14}$$

where the subindices L and R denote values at the interface $r = r_0 + (i + \frac{1}{2})\Delta r$ as calculated from the information at the cell centres i and $i+1$, respectively. With this prescription, two fluxes are found at each cell interface. We proceed to explain how to combine these two flux estimates F_L and F_R at timestep n at an interface, to find one flux at the intermediate time.

2.4. Roe solver

The interaction between the fluid in two adjacent cells is approximated by looking at the resolution of an initial discontinuity at the cell interface. This *Riemann problem* is not solved analytically here. Instead it is approximated numerically by means of a specially chosen linearised form, requiring less computational effort. The loss in precision of the solution is not so bad, because the model of the flow within a cell is generally not completely accurate either. In Cartesian hydrodynamics, for example, one usually supposes the variables to be constant or to change linearly (in some very complex codes even quadratically) within a cell, whereas in reality they are likely to be much more complicated fields. Above, the solutions within a cell were found by assuming stationary flow. This may not be the case in reality, but it is certainly more physical than imposing a preconceived functional form just for mathematical expedience. The fact that, in general, $\partial W/\partial t \neq 0$, is "known" to the code because $F_L \neq F_R$, and the prescription for averaging these two flux estimates restores the evolution. In this sense, our flux estimates (2.13–14) generate the "most stationary" solution.

The central idea of Roe's approximate Riemann-solver is to linearise the Riemann problem in such a way that the correct velocity is found if the initial discontinuity is a pure contact discontinuity or a pure shock. Consider two states respectively

left (L) and right (R) of an interface. First assume that these states are left unaltered for half a time step and calculate the characteristic velocities of a special average of the two states (see Appendix A, eq.(A.1)). The difference between the two states is then decomposed into a part associated with each characteristic velocity. Knowing this decomposition, the flux at the interface half a time step later may be found by tracing back the parts of the flux associated with each characteristic velocity along the path in spacetime defined by that velocity from the interface at the intermediate time step to some place in one of the bordering cells at the present time. For a first order method, only the sign of the characteristic velocities is needed. For a higher order method information of other cells must be used too. Since the emphasis in this article is on the astrophysical results, we will just mention the formulae needed to reproduce the numerical results. The derivation of these can be found in Roe (1981, 1986) or Eulderink (1990).

The essence of Roe's method is, given two states left (L) and right (R) of an interface, to find the eigenvectors e_k and eigenvalues λ_k such that the existence of a state difference

$$W_R - W_L = \sum_k a_k e_k, \tag{15}$$

guarantees that the flux difference obeys

$$F_R - F_L = \sum_k b_k e_k, \tag{16}$$

$$b_k \equiv \lambda_k a_k. \tag{17}$$

Here λ_k is to be identified with the k^{th} characteristic speed and a_k the k^{th} projection coefficient of the state difference on the eigenvectors. The importance of this relation is that if only one $a_k \neq 0$, it is the Rankine-Hugoniot jump condition that holds for *exact* solutions. Thus for a discontinuity in only one Riemann invariant, Roe's method finds the correct characteristic speed.

The first order estimate of the flux at the intermediate time is approximated in Roe's method by

$$F^{n+\frac{1}{2}}_{i+\frac{1}{2},j} = \frac{1}{2}(F_L + F_R) - \frac{1}{2}\sum_k \sigma_k \lambda_k a_k e_k, \tag{18}$$

where $\sigma_k \equiv \mathrm{sign}(\lambda_k)$. A flux like this, being determined by information that has yet to reach the point for which the flux is predicted, is called an upwind flux for physically obvious reasons.

For applications in which source terms are present, we face the difficulty that only the flux is determined by (2.13) and (2.14) and not the state. To determine the state from the flux is numerically expensive because in general more than one state corresponds to a given flux. Not having the state at the interface available is not so much a problem in determining the projection coefficients, because of the relation (2.17). However it is a problem in determining the eigenvalues and eigenvectors. Fortunately, these are only needed to first order in a second order scheme. Therefore we have determined the eigenvectors and eigenvalues based upon the known states at the cell *centres* and then projected the flux differences at the *interfaces* on them.

2.5. Flux limiter

To minimise numerical diffusion one should make the method second order accurate in regions of smooth flow. This may be done by replacing σ_k by $\nu_k = \lambda_k \Delta t/\Delta r$ for the radial integration and by $\nu_k = \lambda_k \Delta t/\Delta\theta$ for the polar integration. However, using this expression near discontinuities will cause unphysical oscillations. To get the best of both worlds a flux limiter is used. This is a function which decides whether it is more likely to be correct to assume a discontinuity between the two states L and R or to assume a smooth transition. Here we have followed Roe's suggestion (Roe 1985), in which one uses the ratio of the state difference at the interface ($a_0 = [a_k]_{i+\frac{1}{2},j}$) to the upwind state difference

$$a_u = \begin{cases} [a_k]_{i-\frac{1}{2},j}, & \text{if } \lambda_k \geq 0 \\ [a_k]_{i+\frac{3}{2},j}, & \text{if } \lambda_k < 0, \end{cases} \tag{19}$$

to decide:

$$\begin{aligned} &\psi(a_0, a_u) = \\ &\quad \max(0, \min(2a_u, \max(a_0, \min(a_u, 2a_0)))) \\ &\quad + \min(0, \max(2a_u, \min(a_0, \max(a_u, 2a_0)))). \end{aligned} \tag{20}$$

The required flux follows from

$$\begin{aligned} F^{n+\frac{1}{2}}_{i+\frac{1}{2},j} =& \frac{1}{2}(F_L + F_R) \\ &- \frac{1}{2}\sum_k \left[\sigma_k a_k + \psi(a_k, a_{ku})(\nu_k - \sigma_k)\right]\lambda_k e_k. \end{aligned} \tag{21}$$

This equation replaces the first order accurate Eq.(2.18). If the state difference is constant, smooth flow is the likely interpretation of the data. As can be easily checked, in that case $\psi(a_0, a_u) = a_0$ and the correct formula for smooth flow is retrieved. If $a_u/a_0 << 1$, one finds $\psi(a_0, a_u) \approx 0$, so that the correct limit for a discontinuity is obtained.

Because we do not have the state differences available at the interface, this formulation is replaced by the equivalent expression

$$\begin{aligned} F^{n+\frac{1}{2}}_{i+\frac{1}{2},j} =& \frac{1}{2}(F_L + F_R) \\ &- \frac{1}{2}\sum_k \left[\sigma_k b_k \right. \\ &\left. + \frac{1}{\lambda_{ku}}\psi(\lambda_{ku} b_k, b_{ku}\lambda_k)(\nu_k - \sigma_k)\right] e_k. \end{aligned} \tag{22}$$

Special care must be taken not to divide zero by zero if $\lambda_u = 0$.

2.6. Source terms

The interface flux is hereby determined. To be able to integrate the equations in the flux-splitting approximation, we must identify which part of the source term belongs to a particular coordinate direction. For the radial direction one has

$$\langle W\rangle^{n+1}_{i,j} = \langle W\rangle^{n}_{i,j} + \frac{\Delta t}{\Delta r}\left(F^{n+\frac{1}{2}}_{i+\frac{1}{2},j} - F^{n+\frac{1}{2}}_{i-\frac{1}{2},j}\right) + \Delta t R^{n+\frac{1}{2}}_{i,j}. \tag{23}$$

Notice how the last two terms can be interpreted as a numerical integration of the fluxes from the left and right interfaces to the cell centre; these are the inverse of Eqs.(2.13) and (2.14).

Because the source term at $t_{n+\frac{1}{2}}$ is unknown, this formula is split into two steps. First an update $\langle W^*\rangle$ of the mean cell state is determined using the source term at the n–th time step

$$\langle W^*\rangle^{n+1}_{i,j} = \langle W\rangle^{n}_{i,j} + \frac{\Delta t}{\Delta r}\left(F^{n+\frac{1}{2}}_{i+\frac{1}{2},j} - F^{n+\frac{1}{2}}_{i-\frac{1}{2},j}\right) + \Delta t R^{n}_{i,j}, \tag{24}$$

and from this update a source term R^* is calculated, which is used to correct the updated state

$$\langle W\rangle_{i,j}^{n+1} = \langle W^*\rangle_{i,j}^{n+1} + \frac{1}{2}\Delta t\left((R^*)_{i,j}^{n+1} - R_{i,j}^{n}\right). \tag{25}$$

Equation (2.24) may be rewritten by combining Eqs.(2.13), (2.14), and (2.22):

$$\begin{aligned}\langle W^*\rangle_{i,j}^{n+1} =& \langle W\rangle_{i,j}^{n} \\ &+ \frac{1}{2}\frac{\Delta t}{\Delta r}\Bigg[\sum_k \Bigg\{(1-\sigma_k)b_k e_k \\ &\quad - \frac{1}{\lambda_{ku}}\psi(\lambda_{ku}b_k, \lambda_k b_{ku})(v_k - \sigma_k)e_k\Bigg\}_{i+\frac{1}{2},j} \\ &- \sum_k \Bigg\{(-1-\sigma_k)b_k e_k \\ &\quad - \frac{1}{\lambda_{ku}}\psi(\lambda_{ku}b_k, \lambda_k b_{ku})(v_k - \sigma_k)e_k\Bigg\}_{i-\frac{1}{2},j}\Bigg].\end{aligned} \tag{26}$$

Numerical tests showed that the correction step (2.25) hardly affects the flow. Therefore it was omitted to save computer time.

Although the actual Roe-solver is only a part of the whole method, it is the most essential part. Therefore we designate the whole method by that name, including the flux splitting and the subgrid method introduced by Eulderink (1990). The Roe-solver, in this broad sense, consists of finding one-dimensional updates using Eqs.(2.24) and (2.25). The fluxes are found using Eq.(2.22), which uses the left and right fluxes as defined in Eqs.(2.13) and (2.14). The explicit expressions for the eigenvalues λ_k, eigenvectors e_k, and projection coefficients b_k appearing in these equations, are given in Appendix A. The flux splitting technique, as described in Sec.2.1, is used to obtain two-dimensional updates.

To test our method (in addition to the usual shock tube verifications), we used the 'windtunnel with step' problem (cf. Woodward & Colella 1984). The result of this can be found in Appendix B. This test shows how well the Roe solver handles complex shock structures on a cartesian grid. To test it on a spherical grid we compared our results to the analytical self-similar solutions for the interacting winds problem given by Chevalier & Imamura (1983). The two solutions agree well. The numerical values come within 10 % of the analytical ones.

3. Initial and boundary conditions

3.1. The grid and the boundary conditions

As we motivated above, we choose spherical coordinates (r, θ). Because of the symmetry conditions we only need to model one quarter of the plane of constant ϕ, so θ runs from 0 at the polar axis to $\pi/2$ at the equatorial plane. This interval is filled with cells of constant angular size $\Delta\theta$. This implies $\theta_0 = -\Delta\theta/2$.

In the radial direction our grid does not extend all the way to $r = 0$, but starts at $r = r_0$. This radius r_0 is the distance from the star at which the interaction of the fast wind and slow wind begins, so if v_0 and v_c are the velocities of the slow and fast wind, $r_0\left(1/v_0 - 1/v_c\right)$ is a measure of the interval between the time at which the slow wind switches off, and the time at which the fast wind switches on. The radial cell length is Δr. Thus, the grid is determined by the number of grid points in the radial and tangential directions, the radial cell size Δr, and the inner boundary radius r_0.

Putting the edge of the grid at the interaction radius, means that we cannot follow in detail the evolution of the inner shock, since it almost instantaneously runs off our grid. But since the actual nebula we try to model is associated with the outer shock, this is not a severe problem. In fact, it would require a very large grid to catch both the inner and outer shock on one grid, so a choice has to be made.

This of course leads to the problem of how to conserve the dynamical influence of the fast wind. Clearly, we cannot let the inner shock just run off our grid, because then there would be nothing left to drive the interaction. As a first attempt one could keep the fast wind fixed in the first row of cells, without letting this row of cells evolve. This in the long term leads to instabilities at this inner boundary.

We decided to put in the conditions of a stationary shock. The first row of cells still contains the fast wind condition, but this serves as a dummy row since it is kept fixed together with the second row, which contains the shocked fast wind. This row of cells interacts with the slow wind which fills the third and subsequent rows (see Sec.3.2). This configuration works fine, and even succeeds in modelling the inner shock. If the pressure in the hot bubble falls below the pressure of the shocked wind, a shock starts travelling into the grid, which in position and speed closely matches the inner shock as described by the analytical (self-similar) models of Chevalier & Imamura (1983). This is an illustration of the fact that pressure driven winds are numerically easier to model than velocity driven winds. The stationary shock transforms kinetic energy into thermal energy, for a strong shock and $\gamma = 5/3$, $3/4$ of the kinetic energy is thermalised.

The fast wind is assumed to be spherical and is determined by constant speed v_c, constant temperature T_c and constant mass loss. This means that the density $\propto r^{-2}$, where we take $\rho = \rho_c$ at $r = r_0$. The shocked wind in the second row of cells satisfies the Rankine-Hugoniot conditions for a stationary shock (e.g. Landau & Lifshitz 1987, §89):

$$\begin{aligned}\rho(i=2) &= \frac{(\gamma+1)\mathcal{M}_c^2}{\gamma\mathcal{M}_c^2+2}\rho_c \equiv \eta\rho_c, \\ \rho v_r(i=2) &= v_c/\eta, \\ e(i=2) &= e_c = \rho_c\frac{k}{m_p}T_c + \frac{1}{2}\rho v_c^2,\end{aligned} \tag{27}$$

with $\mathcal{M}_c$ the Mach number of the fast wind. This configuration supplies an inner boundary condition; the fast wind is determined by the three parameters ρ_c, v_c, T_c.

At the outer radial boundary we use upwind linear extrapolation to estimate the state in a virtual cell outside the grid:

$$W_{m+1}^n = W_m^{n+1} = (v_r\Delta t/\Delta r)W_{m-1}^n + (1 - v_r\Delta t/\Delta r)W_m^n, \tag{28}$$

with W the state vector. This is valid as long as there is outflow across this boundary.

The boundary conditions at the symmetry axis follow from the rotation symmetry, and since $\sin\theta$ is zero on the axis, the flux on the axis should be taken zero. At the equatorial plane, the boundary conditions follow from reflection symmetry.

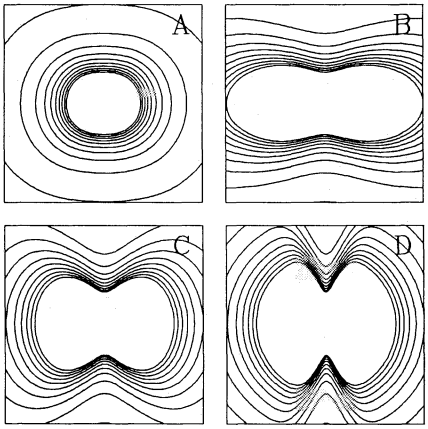

Fig. 1. The initial density distribution. Linear isodensity contours in rectangular coordinates for $A = 0.3$, $B = 1.0$ (top left), $A = 0.9$, $B = 1.0$ (top right), $A = 0.8$, $B = 3.0$ (bottom left), and $A = 0.8$, $B = 12.0$ (bottom right). We use $\alpha = 2$

3.2. *Initial conditions*

We choose the following initial condition for the slow wind. At $t = 0$ the whole grid except the first two rows (which contains the fast wind inner boundary conditions defined above), is filled with the aspherical slow wind. Along the symmetry axis this wind has a radial density distribution

$$\rho(r) = \rho_0(r_0/r)^\alpha, \tag{29}$$

and the tangential dependence for the rest of the grid follows from

$$f(\theta) = 1 - A\left(\frac{1 - \exp(-2B\sin^2\theta)}{1 - \exp(-2B)}\right), \tag{30}$$

to give

$$\rho(r,\theta) = \frac{\rho_0}{f(\theta)}(r_0/r)^\alpha. \tag{31}$$

The tangential velocity in the slow wind is zero everywhere. The radial velocity is found from the assumption of constant mass loss $\dot{M}_{\rm RG}$:

$$v_r(r,\theta) = v_r(r_0,\theta)(r_0/r)^{2-\alpha}, \tag{32}$$

$$v_r(r_0,\theta) \equiv v_0 f^\beta(\theta). \tag{33}$$

The formulation for $f(\theta)$ was devised by I 88 and has the advantage of always giving smooth contours at the axes (which the other often used possibility, $f(\theta) = 1 - A(1 + \cos^\alpha\theta)$, for α an odd integer, does not have). The quantity A lies between 0 and 1, and regulates the density contrast; the parameter B governs the rate at with which the density changes with angle. The density ratio between equatorial and polar direction (e/p ratio) equals $1/(1 - A)$. Low B gives density distributions with high values near the equator and low values in the rest of the grid, corresponding to a thin disk, high B values give density distributions with high values in the whole grid except very near the pole. This configuration is often called a thick disk and the polar density depression is called a funnel. As an illustration, we show in Fig.1 the resulting isodensity contours for the four combinations of A and B used in Fig.2.

Along the symmetry axis ($j = 1$) the temperature is found from Bernoulli's equation

$$T(r) = \frac{\gamma - 1}{2\gamma}\frac{m}{k}(v_o^2 - v_r^2(r, j = 1)) + T_0. \tag{34}$$

For $\alpha > 2$ this formulation can give negative temperatures, but all models discussed in this article have $\alpha = 2$, so this isn't a problem. For the rest of the grid the temperature follows from the demand of pressure equilibrium in the tangential direction

$$T(r,\theta) = \frac{T(r, j = 1)\rho(r, j = 1)}{\rho(r,\theta)}. \tag{35}$$

This is done to rule out any tangential flows in the slow wind at the beginning of the integration.

In summary, the slow wind is determined by seven input parameters: ρ_0, α, A, B, v_0, β, T_0. The prescription of asphericity (Eqs.(3.4–5)), is chosen for consistency with the analytical models of I 88 and to compare our results with the numerical models of IBF 91.

These initial conditions are an idealisation of the true initial conditions for a PN, which are as yet unknown from direct observations. Typical estimates found in the literature hold that an AGB-wind of about 10^{-7} $M_\odot$ yr^{-1}, is probably followed by one or maybe more bursts of superwinds of 10^{-4}–10^{-5} $M_\odot$ yr^{-1}, after which there may or may not follow an intermediate wind, followed by the fast wind.

The detailed properties of these winds, especially the dependency on initial mass and the behaviour in time, are too uncertain to justify more detailed modelling. Instead of that, we aim here at more generic models, which show the possible configurations in the interaction between a spherical fast wind and an aspherical slow wind.

One final remark about the parameters employed. Although we have used, and will continue to use below, specific plausible values for physical quantities such as the wind mass flux, velocity, density, and so forth, one should note that our models can be scaled in various ways. Every scale transformation of the equations of motion (2.1–5) is implicitly allowed. Such scaling will be necessary when making detailed comparisons with actually observed nebulae (see IBF 91 for a detailed discussion).

4. Results and discussion

In this section we show some results of the numerical work we have done. Our computer runs have covered the parameter space of the family of initial conditions described above. Most of these used a 50×50 grid, some a 100×100 grid. All calculations were performed on the Convex C-210 of the University of Leiden. Our fully vectorised code took 37.6 microseconds per grid point and per timestep. These runs give us a good impression of the effects of different initial density distributions.

4.1. *The effect of different initial density distributions*

Our results agree with the conclusion of I 88 that one needs a steep dependence on θ in $\rho(\theta)$ to get extremely aspherical nebulae. Most forms obtained show almost spherical, via elliptical, to figure-eight type forms. In Fig.2 we collect a few examples of the

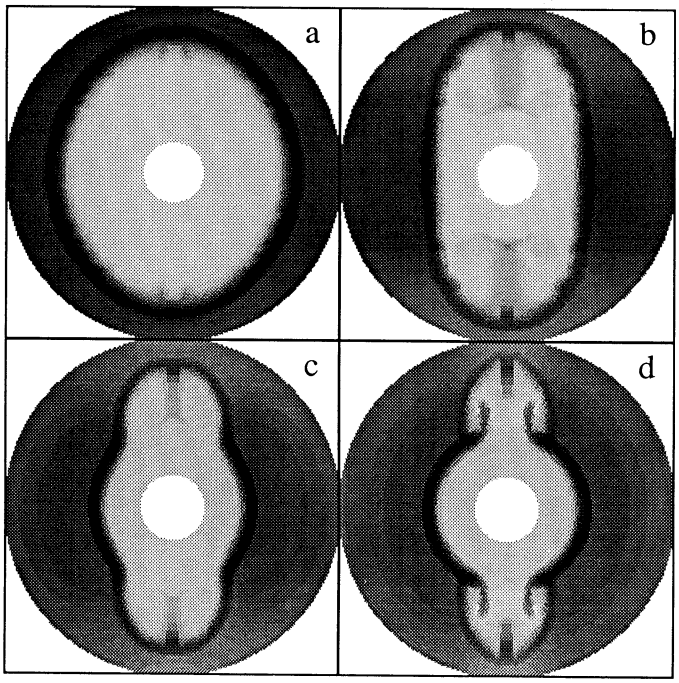

Fig. 2. A collection of morphologies found. The frames show mass density plotted in logarithmic greyscales, darker shades expressing higher values. The computational results have been transformed from spherical to rectangular coordinates. The symmetry axis runs vertically, the equatorial plane horizontally. Clockwise from the top left, bubbles with (a) $A = 0.3$, $B = 1.0$ (almost spherical), (b) $A = 0.9$, $B = 1.0$ (elongated, peanut shaped), (c) $A = 0.8$, $B = 3.0$ (with mild cusp), (d) $A = 0.8$, $B = 12.0$ (with cusp folding, jet formation). Times are 285 years for (a) and (b) and 317 years for (c) and (d). The grid of (a) and (b) extends to $r = 5.84 \times 10^{14}$ m $= 0.019$ pc, of (c) and (d) to $r = 1.785 \times 10^{15}$ m$= 0.058$ pc. Other input parameters are $\rho_0 = 3.0 \times 10^{-17}$ kg m^{-3}, $\alpha = 2$, $v_0 = 1.0 \times 10^4$ m s^{-1}, $\beta = 0.001$, $T_0 = 3.0 \times 10^3$ K, $\rho_c = 1.0 \times 10^{-21}$ kg m^{-3}, $v_c = 2.0 \times 10^6$ m s^{-1}, $T_c = 5.0 \times 10^4$ K, $r_0 = 3.0 \times 10^{14}$ m, for (a) and (b), and $\rho_0 = 3.0 \times 10^{-17}$ kg m^{-3}, $\alpha = 2$, $v_0 = 1.0 \times 10^4$ m s^{-1}, $\beta = 0.001$, $T_0 = 3.0 \times 10^3$ K, $\rho_c = 1.0 \times 10^{-20}$ kg m^{-3}, $v_c = 2.0 \times 10^6$ m s^{-1}, $T_c = 5.0 \times 10^4$ K, $r_0 = 3.0 \times 10^{14}$ m, for (c) and (d)

different forms found, obtained from four different 50×50 runs. The figures show logarithmic greyscale plots of the mass density. The results have been transformed from the computational (r, θ)–grid to a rectangular (R, Z)–grid, to give an idea of their observational appearance.

Here and in the rest of the paper we use logarithmic greyscale plots to illustrate our results. Darker shades correspond to higher values. Taking the logarithm enormously increases the dynamic range of the plots. A linear plot of for instance the density would only show the densest parts. This should be kept in mind when interpreting the plots.

It is striking that for θ–values for which the outer density distribution is more or less spherical, the shock also stays spherical to a high degree. The deviation from sphericity appears to be just superposed on this spherical part; the angle at which the deviation starts depends on B. Thus one can split the configuration into two parts, a spherical part (for high θ) and a 'protruding' part (for low θ). At the position of transition from the spherical part to the protruding part, the shape of the shock may alter smoothly (for low B–values, $B < 2$), or with a cusp.

The dependence on A is much weaker, as expected from the analytical work. For larger A, the ratio of the shock position at the pole to that at the equator increases. The effect on the shape of the shock between pole and equator depends mainly on B. For low B and low A values ($B < 2$, $A < 0.4$, (e/p)< 1.7), the shock form does not differ much from spherical (Fig. 1a). For low B ($B \simeq 1$) and high A ($A \geq 0.7$, (e/p)> 3.0) the form of the shock is an elongated round figure (Fig.2b). Intermediate B ($2.0 < B < 5.0$) and high A values result in a spherical component with something like an ellipse on top, separated by a cusp (Fig.1c). For high B ($B > 5.0$) and high A values the cusp breaks up and the inside of the protruding part adopts a jet-like appearance (Fig.1d), which will be discussed in Sec.4.4.

In order to look in more detail at the structure of the bubble, we take two examples of higher resolution runs, one with $B = 1.0$ and one with $B = 6.0$. The rest of the input parameters is the same for both models: $A = 0.9$, so (e/p)$=10.0$, $\rho_0 = 1.0 \times 10^{-16}$ kg m^{-3}, $\alpha = 2$, $v_0 = 1.0 \times 10^4$ m s^{-1}, $\beta = 0.0001$, $T_0 = 3.0 \times 10^3$ K, $\rho_c = 2.2 \times 10^{-21}$ kg m^{-3}, $v_c = 2.0 \times 10^6$ m s^{-1}, $T_c = 5.0 \times 10^4$ K, $r_0 = 3.0 \times 10^{14}$ m. This corresponds to a transition time of ~ 1000 yr between the two winds and mass losses $\dot{M}_{RG} = 1.8 \times 10^{-5}$ M$_\odot$ yr^{-1} (at the pole) and $\dot{M}_{FW} = 7.8 \times 10^{-8}$ M$_\odot$ yr^{-1}. The radial cell size is 3.0×10^{13} m, so the 100×100 grid extends to 3.285×10^{15} m (0.106 pc).

Figure 3 shows greyscale plots of mass density, (absolute) velocity with a vector overlay of velocity direction, temperature, and pressure, at $t = 5.0 \times 10^{10}$ s ($= 1.6 \times 10^3$ yr), for the $B = 1.0$ run. Figure 4 shows the same for the $B = 6.0$ run.

Note that the vectors in the velocity plot *only* give the direction. The length of the arrows is constant. The underlying greyscale plot of the velocity shows the magnitude. This representation is chosen because the standard way of plotting the velocity field (using arrows whose length indicates the absolute value), in this case easily leads to vectors crossing each other and extending much beyond their actual location, resulting in very unclear plots (cf. Fig.5 of Soker & Livio 1989).

In the plot of the mass density one sees the high density shell, where densities increase with θ, since the outer density is higher there. Because this is all swept-up slow wind material, the contrast in the shell roughly corresponds to the contrast in the slow wind. Inside the bubble the density structure is dominated by an area of higher density along the symmetry axis. This axial condensation is interacting with the swiftly outflowing gas to produce vortex cascades. At the outer shock the condensation is highest, for the $B = 6.0$ case there is also a condensation maximum further inward.

In the plots of the absolute velocity one sees high values in the protruding part of the bubble. This shows a collimation of the stream in the direction of least resistance. This is also clearly visible from both vector plots: the streamlines deflect from the high density equatorial layers and seek their way into the protruding part.

In the high B case one sees that the gas is forced to flow towards the symmetry axis by the extensive equatorial belt. Part of this stream, once beyond the cusp, again deflects and starts flowing away from the symmetry axis. This flow may lead to the formation of a complex structure around the cusp, which is just beginning in this case. This phenomenon will be further discussed in Sec.4.4. The bulk of the gas flows into the protruding part of the bubble, going around the axial condensation, strongly interacting with it. At the constrictions near the cusp and in the upper part of the bubble, the gas attains higher velocities.

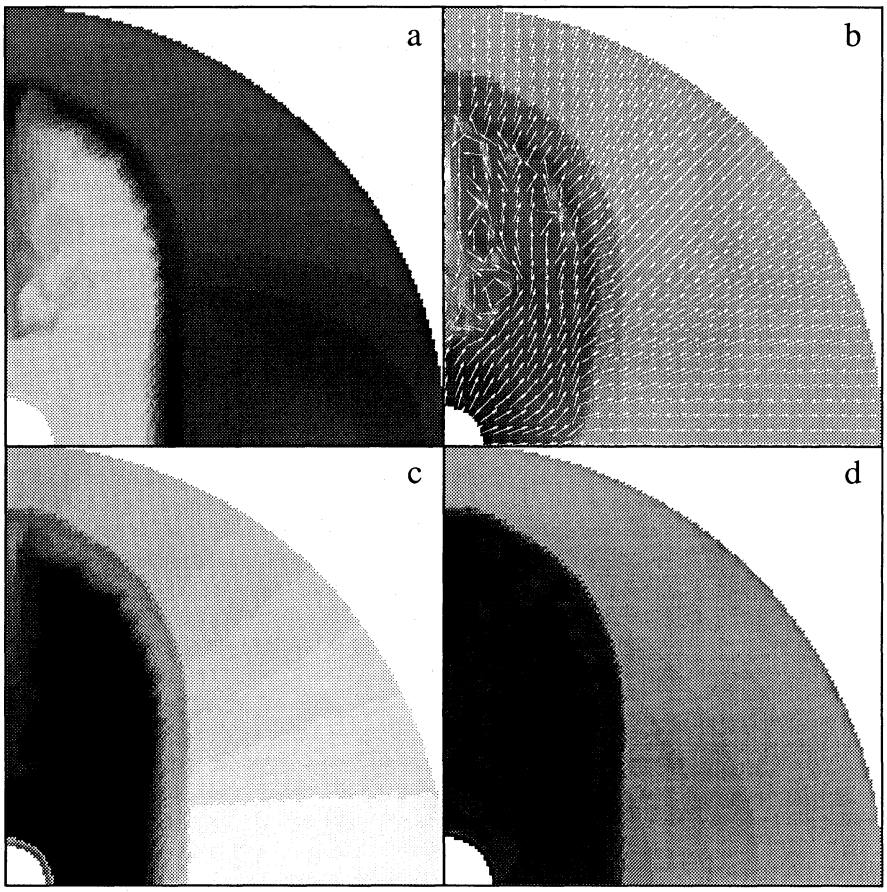

Fig. 3. A $A=0.9$ $B=1.0$ bubble at t = 1584 years. The frames are in rectangular coordinates, showing one quarter of the whole plane. The symmetry axis is the left vertical axis. The frames contain logarithmic greyscale plots of the mass density (a), absolute velocity with direction overlay (c), temperature (c), and pressure (d). The outer edge of the frames is at $r=3.285\times10^{15}$ m = 0.106 pc

In the low B case the confining equatorial belt does not extend as far as in the high B case, and the gas can just flow straight up and is thus less collimated, as is clear from the vector plot. Here also the gas flows around the axial condensation, interacting with it.

It is striking that the velocity starts to deviate from spherical outflow much nearer to the equator than the density contours suggest. So, although the form of the shock suggests that only below a certain θ–value deviation from spherical structure occurs, the velocity shows that inside the bubble the flow is non-spherical for much higher values of θ.

The structure in the temperature is rather simple. Inside the shell there is a hot bubble of almost 10^8 K. This has a uniform distribution, apart from the cool feature along the axis. The shell itself is much cooler (10^5–10^6 K) where the denser parts are the coolest. This corresponds to a more or less uniform pressure distribution behind the outer shock, as can be seen from the pressure contours. The total energy density more or less follows the mass density distribution.

Finally, we show in Fig.5 the development in time of the density contours of the bubble of Fig.4.

One sees how the asphericity increases with time, since the ratio of shock positions at pole and equator increases. But besides this, the general structure of the bubble is more or less constant and as described above.

4.2. Comparison with analytical and numerical work

I 88 presents in his Fig.12 shock configurations for $\delta = 0.1$, $\sigma = 2$, 4 and 8 at different times τ. These parameters correspond to ours according to $A = 1-\delta$, $B = 0.5\sigma$, and $\tau = t\sqrt{(\gamma+1)\rho_c v_c^2/(2\rho_0 r_o^2)}$. This means that our Fig.3 shows a $\delta = 0.1$, $\sigma = 2.0$ bubble at $\tau = 1.78$ (Fig.4 has $\sigma = 12.0$).

One sees that the analytical and numerical shock figurations match very well. The bubble is undergoing the transition from an elongated shape (at $\tau = 1.5$) to a peanut shape (at $\tau = 2.0$). The ratio between polar and equatorial shock position is 2.4 in the analytic calculations, and 2.0 (Fig.3) in the numerical ones, a discrepancy of 17%. Considering the enormous differences between the two approaches, this is a very good result.

Unfortunately the larger τ values are beyond our reach until more computer time becomes available.

Our results also correspond reasonably well with the earlier phases of Soker & Livio (1989). As was explained in Sec.1 their code suffers from a lot of diffusion which mainly affects the later evolutionary stages. Comparison of our Figs.3 and 4 with theirs shows that, the interesting morphological features of the flow can barely be discerned, in particular at the cusp.

4.3. Axial condensations

As already became clear in Sec.4.1, there is one striking feature in our models, namely that of a density enhancement at the symmetry axis. This material is moving slower than the bulk of the outflowing material, sometimes actually flowing back. There is interaction with the outflowing material, resulting in vortex cascades. In all cases the bubble stays roughly isobaric, so the temperature of the condensation is lower than that of the surrounding gas. Examples of this feature can be found in all figures of this article.

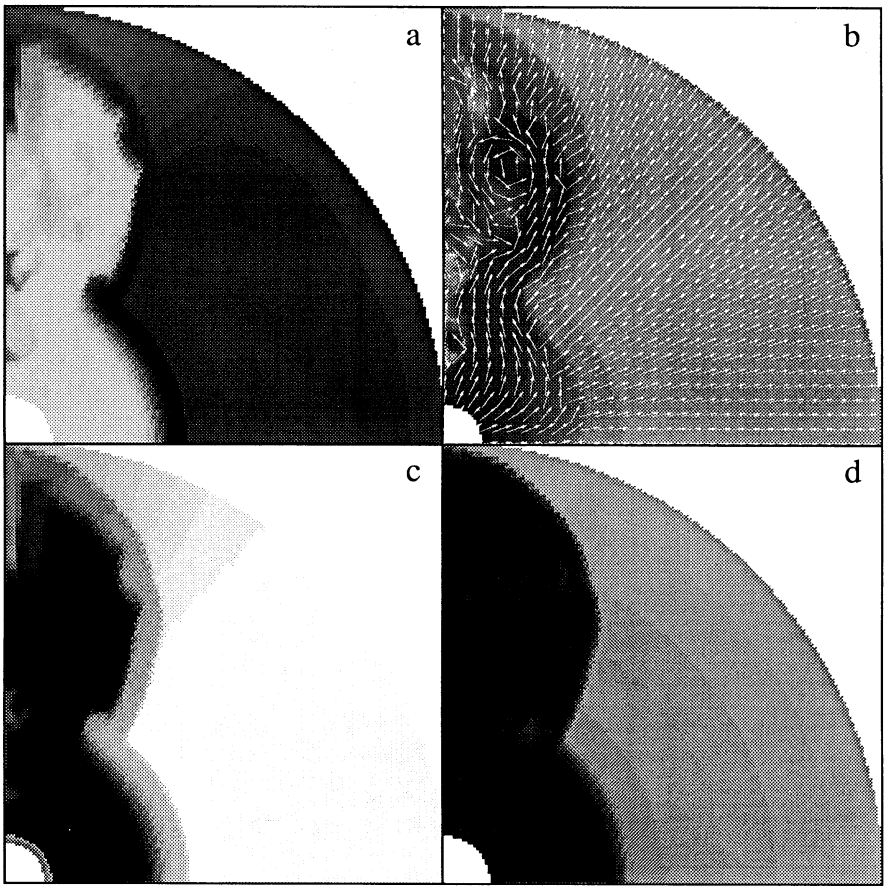

Fig. 4. As Fig.3, but for $A = 0.9$, $B = 6.0$.

We found that the two main parameters determining the formation of these condensations are the density ratio between pole and equator, or A, and the ratio between outer and inner density, ρ_o/ρ_c. The condensation becomes more pronounced for higher A and larger ρ_o/ρ_c. In Fig.2a (both parameters low), almost no condensation is seen, in Figs.3 and 4 (both parameters high), the condensations become very noticeable.

These regions of higher density form a problem. Since they occur on the axis of our grid, they are suspect: they could be the result of numerical errors. Because the metric changes quickly there ($\propto \sin\theta$), one can expect problems.

We have tried several things to remove this suspect feature. We changed the flux limiter, added metric correction factors to the flux, changed the source term splitting (eqs.(2.11-12)), all without noticeable effects on the axial condensation. We looked at the purely spherical initial condition ($A = 0.0$), but there it did not show up. We searched for strange features when there is a strong tangential velocity in a spherical metric; there were none. All this seems to indicate that the effect is not caused by errors in the numerical method. The strongest evidence that it is a real effect is the fact that the same effect occurs even when the direction of lowest density is not the polar direction. We tried runs using $\sin(\theta - \pi/4)$ and $\cos\theta$ instead of $\sin\theta$ in equation (3.4), and in both cases a similar high density feature appears in the protruding part.

It is of course true that that our strict mathematical condition of axi–symmetry at the polar axis inhibits any real physical (3–D) interaction between the different gas flows converging here from different parts of the bubble. Any tangential flow is stopped dead at the axis, which naturally leads to condensations. Similar types of axial condensations have been found in other axi–symmetric calculations (MacLow et al. 1989; Soker & Livio 1989; Norman et al. 1983).

As was noted by the referee, in the case of a rising air bubble in water, axi–symmetric calculations show phenomena on the axis which are not found in experiments. In these experiments the bubble wobbles, an action inhibited by the symmetry condition in the calculations. Whether a similar effect is going on in our case is a question which cannot be answered without doing full three dimensional calculations. Unfortunately, this must wait until computers have become some two orders of magnitude faster.

Meanwhile we can conclude that we find that material from the inside of the bubble is focussed toward the axis. There it interacts with material coming fom the other parts of the bubble. Our choice for axi–symmetry leads to the formation of axial condensations of low velocity (even back flowing). In reality this interaction may result in such condensations, but might also resolve into non–axial flow patterns.

It is tempting to try and identify these condensations with features in PNe, such as the ansae, as indeed Soker & Livio (1989) did. But in view of the above and the fact that they are found inside the bubble (in contrast to the observations), such an interpretation would seem premature.

4.4. Behaviour at strong cusps

In our simulations another special feature occurred, this time at a place where it could be expected, near the cusp in the outer shock.

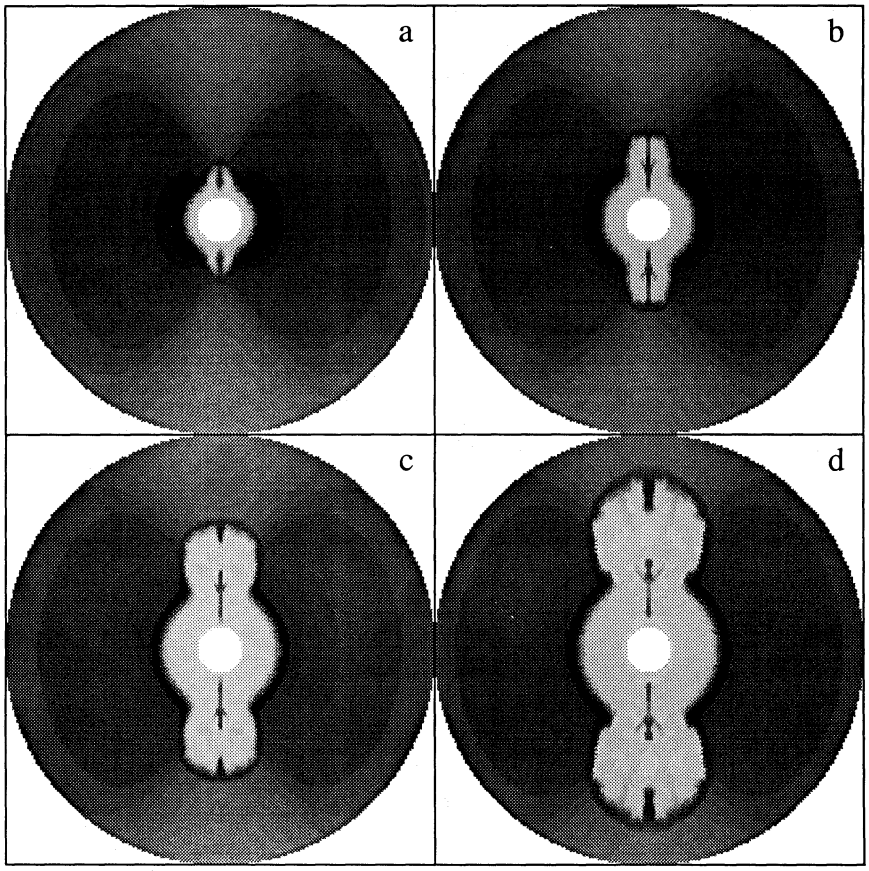

Fig. 5. Development in time of the $A = 0.9$, $B = 6.0$ bubble of Fig.4. The frames show logarithmic greyscales plots of the mass density in the whole plane in intervals of 317 years. (a) $t = 475$ yr, (b) $t = 792$ yr, (c) $t = 1109$ yr, (d) $t = 1426$ yr. The plots in Fig.4 are at $t = 1584$ yr

I 88 stated that for strong cusps (regions where $\partial x/\partial\theta$, with x the shock position, is very large) his analytical approximation might break down. We find that this is not actually the case, but inside of the outer shock something special does happens. For values of B greater than 5–6 and A greater than 0.6, we find that after some time the cusp in the outer shock starts to break up into two parts.

The protruding part folds itself around the spherical part of the shock. This feature starts as a little vortex at the cusp, which then develops into a backflow along the spherical part of the outer shock. The cusp predicted by the analytical work persists in the form of the intersection of the protruding and quasi-spherical parts of the outer shock, but the hydrodynamic structure behind it becomes very complex. It starts as a vortex "curl", which becomes the base of the "chimney" laid down by the sheared-off inner surface of the contact discontinuity.

In Fig.6 one can see the development of such a flow pattern in the density. This run has $A = 0.8$, $B = 8.0$ on a 100×100 grid. The other input parameters are: $\rho_0 = 3.0 \times 10^{-17}$ kg m^{-3}, $\alpha = 2$, $v_0 = 1.2 \times 10^4$ m s^{-1}, $\beta = 0.001$, $T_0 = 3.0 \times 10^3$ K, $\rho_c = 1.0 \times 10^{-20}$ kg m^{-3}, $v_c = 2.0 \times 10^6$ m s^{-1}, $T_c = 5.0 \times 10^4$ K, $r_0 = 3.0 \times 10^{14}$ m. This corresponds to mass loss values of $\dot{M}_{RG} = 6.4 \times 10^{-6}$ $M_\odot$ yr^{-1} (at the pole) and $\dot{M}_{FW} = 3.6 \times 10^{-7}$ $M_\odot$ yr^{-1}.

The origin of this phenomenon seems to be twofold. Before the breaking up of the cusp, one can see how the gas flow, once beyond the cusp, diverges, blowing the protruding part over the spherical part (note the almost horizontal arrows beyond the cusp in Fig.4d). So the protruding part seems to encapsulate the spherical part. On the other hand, material is being dragged off from the contact discontinuity, to form the band of high density material separating the outflow and the backflow. Figure 6 shows this band undulating in the outflowing wind.

In the course of time, this feature can become quite extreme, as Fig.7 shows. Here the protruding part of the bubble has developed into a turbulent cocoon, at the inside of which a jet-like structure can be seen, which collimates very well. One can even discern the X-type shocks and chambers that are typical of jet simulations (Norman et al. 1983).

This dragging along of the contact discontinuity into the hot bubble cap is a novel feature produced in our calculations, and is also found by IBF 91. Notice the superb collimation of the hot flow. The opening angle of the funnel in the initial density distribution is about 50°, whereas the opening angle of the resulting jet is close to zero. The excellent collimation of the inner flow was not entirely anticipated. The flow is not collimated by the Blandford & Rees (1974) "nozzle" mechanism; instead, the gas which is scraped off the contact discontinuity travels along with the stream and forms a hollow structure. Evidently, the hot gas is collimated very well by this mechanism, even though the appearance of the outer shock would hardly lead one to suspect the existence of an inner jet-like structure. In fact, the outer shock cannot be collimated very well under any plausible circumstances (I 88). Possibly we see this configuration of a bubble-like outer shock around a tube-like protrusion in the Calabash Nebula (Icke & Preston 1989).

All this suggests that this feature may have other applications

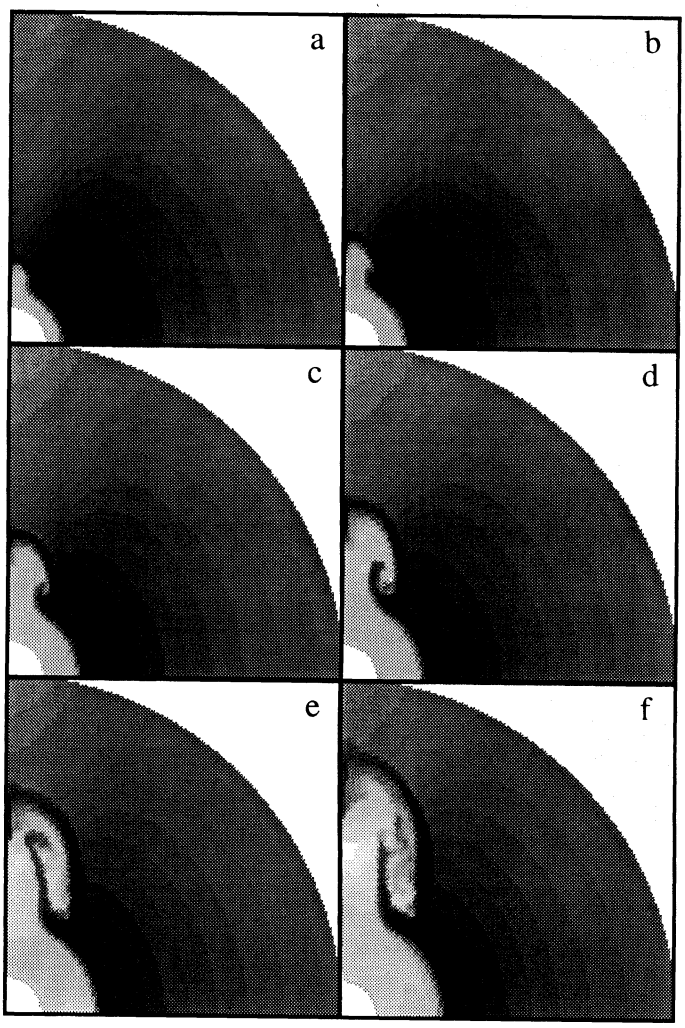

Fig. 6. Development of a cusp. The frames show logarithmic greyscale plots of the mass density in rectangular coordinates of an $A = 0.8$, $B = 8.0$ bubble in intervals of 64 years starting at $t = 158$ yr, ending at $t = 475$ yr. The frames extend to $r = 3.285 \times 10^{15}$=0.106 pc

beside PNe. It shows that a fast wind travelling into a thickened disk-like density distribution can produce jets.

We are confident that this behaviour at the cusp is physical. First of all, it appears at a spot where it was expected; secondly, it develops quite naturally in the hydrodynamical structure. Furthermore, the results of IBF 91 show exactly the same features, obtained by means of a radically different hydrocode.

4.5. Observational Implications

We have seen in the above that the analytical theory is nicely confirmed by the numerical work, as far as the outer shock is concerned. New effects are seen mostly at the contact discontinuity where the hot gas of the shocked fast wind meets the much cooler and denser gas which has passed through the outer shock. This means that the present calculations hardly modify the conclusions reached by I 88 and Icke et al. (1989) about the shapes of PNe and their spectral lines. The reason for this is that the interesting new effects all take place in or very near the hot, tenuous inner cavity of the PN. Because such hot gas is almost invisible optically, these effects will be difficult to observe.

The phenomena between the outer shock and the contact discontinuity (the "snowplow" layer) appear to be understood in our model. The mass which is swept up near the equator has a characteristic barrel shape, the existence of which has long been assumed in models of the free-free radio radiation (see e.g. Zijlstra 1989, and references therein). Even the optical pictures of some aspherical PNe bear a strong resemblance to our simulations: a shell which is denser in the equatorial direction and more elongated in the other (polar) direction (see e.g. NGC 6720 and IC 1454). So, although a detailed comparison cannot be made without full radiative effects, the general outline seems to be well represented by our calculations. This is encouraging and justifies further pursuit of these models.

5. Conclusions

Our main conclusions can be summarised as follows:

1. The Roe-solver as presented by Roe (1981) and extended by Eulderink (1990), is a very good scheme for doing numerical hydrodynamics. It is essentially a simple method that gives very good results for problems containing extreme discontinuities. The advance of computer technology now permits the construction of codes which can crack really hard problems, such as this interacting wind problem.
2. Using a density contrast in the remnants of the AGB-wind, we can model aspherical bubbles of the kind analytically found by I 88 and that were suggested by Balick (1987) as an explanation for aspherical planetary nebulae. These models agree well with the ones found by IBF 91.
3. Although the outer shock looks fairly strictly divided up into a spherical and a 'protruding' part, as was found analytically by I 88, the structure of the bubble inside of the contact discontinuity is much more complicated. This rich structure will be difficult to observe.
4. The transition from the spherical to the protruding part of the outer shock is often characterised by a cusp, especially when the outer density distribution changes quickly with θ. When this cusp becomes too sharp, the protruding part of the outer shock starts to encapsule the spherical part. This gives rise to a cocoon-like configuration or "chimney" around a jet. This feature bespeaks a high degree of collimation of the flow, due to the high density belt at the equatorial plane. It shows that thickened disks can produce jet-like phenomena, albeit by a mechanism different from that introduced by Blandford & Rees (1974).
5. At the polar axis (i.e. in the direction of lowest density in the outer wind) a region of high density and low temperature forms. This region is located just behind the contact discontinuity and can extend a long way into the bubble. The radial velocity is lower. Interactions with the outflowing material produce vortex cascades. The main parameter determining the degree of condensation is the ratio between slow and fast wind density. If this ratio is low, a bubble is quickly blown, and the condensations do not get the chance to develop. If this ratio is high, a lot of material gets focused towards the axis and strong condensations form. It can not be excluded that these condensations are (partly) induced by the use of an axi-symmetric grid. IBF 91 do not find such condensations,

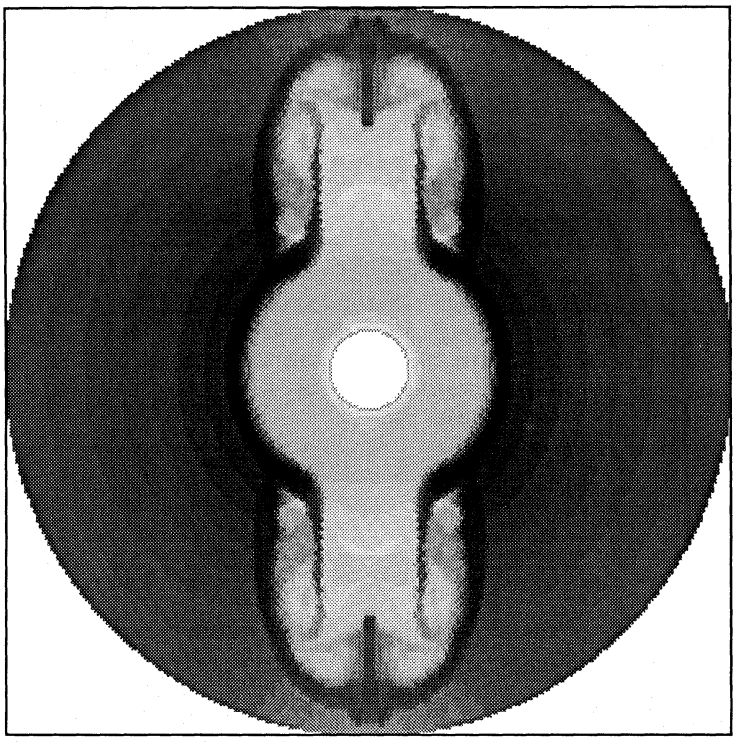

Fig. 7. A fully developed cocoon. A logarithmic greyscale plot of the mass density in rectangular coordinates of the bubble of Fig.6 at $t = 539$ years

but since they only model the low density ratio regime of parameter space, their results are not in contradiction with ours.

6. Our simulations show no direct evidence of the formation of ansae, which are often observed in aspherical PNe.

Since these conclusions follow from adiabatic models, they cannot be applied to PNe without caution. Radiative heating and cooling can change the configuration of the entire bubble. Certainly by changing the appearance, and maybe also by changing the dynamics. The dense shell will cool efficiently and thus become radially thinner and denser. The high temperature bubble will probably not cool very well, but the density enhancement along the axis might. When the outer shock slows down (e.g. due to a decrease of the momentum density of the fast wind), these axial condensations could overtake the shock, producing ansae. Work on the inclusion of radiative effects is in progress.

Acknowledgements. We thank Bruce Balick and Adam Frank for the useful discussions during their visits to Leiden, and Rob van Dijk for supplying his shock tube program for testing the code. We also appreciate the constructive remarks made by our (anonymous) referee. The largest part of the time difference between date of submission and date of acceptance is due to the *A & A* office. G.M. receives financial support from NWO, the Netherlands Organisation of Scientific Research, under grant number 782-372-029. The work of V.I. on planetary nebulae is supported in part by the North Atlantic Treaty Organisation (NATO), under grant number 0898/87.

Appendix A: Explicit expressions

The explicit expressions for the eigenvectors, the coefficients, and the characteristic velocities, are given below in terms of averages, weighted with the square root of the density. For example, the interface value H of the specific enthalpy $h = (e+p)/\rho$ is related to the left– and right-hand quantities (defined in Sec.2) by

$$H \equiv \frac{[\sqrt{\rho}h]_L + [\sqrt{\rho}h]_R}{[\sqrt{\rho}]_L + [\sqrt{\rho}]_R}. \tag{A1}$$

Likewise, V_r is related to $v_r \equiv \mathrm{d}r/\mathrm{d}t$ and V_θ to $v_\theta = \mathrm{d}\theta/\mathrm{d}t$. As was discussed in Sec.2.1, the actual integrations are done separately in the radial and in the polar direction. Below, first the expressions are given for the integration in the radial direction, and then for the integration in the polar direction.

At an interface at (r, θ), the characteristic speeds for the integration in the radial direction are given by

$$\begin{aligned} \lambda_1 &= V_r - s \\ \lambda_2 &= V_r + s \\ \lambda_3 &= V_r \\ \lambda_4 &= V_r, \end{aligned} \tag{A2}$$

where

$$s^2 \equiv (\gamma - 1)\left(H - \frac{1}{2}\left[V_r^2 + r^2 V_\theta^2\right]\right). \tag{A3}$$

The eigenvectors are

$$\begin{aligned} e_1 &= (1, V_r - s, V_\theta, H - sV_r) \\ e_2 &= (1, V_r + s, V_\theta, H + sV_r) \\ e_3 &= (1, V_r, V_\theta, \frac{1}{2}(V_r^2 + r^2 V_\theta^2)) \\ e_4 &= (0, 0, 1, r^2 V_\theta). \end{aligned} \tag{A4}$$

The projection coefficients of a flux difference $F_R - F_L \equiv (\Delta_1, \Delta_2, \Delta_3, \Delta_4)$ in the radial direction are:

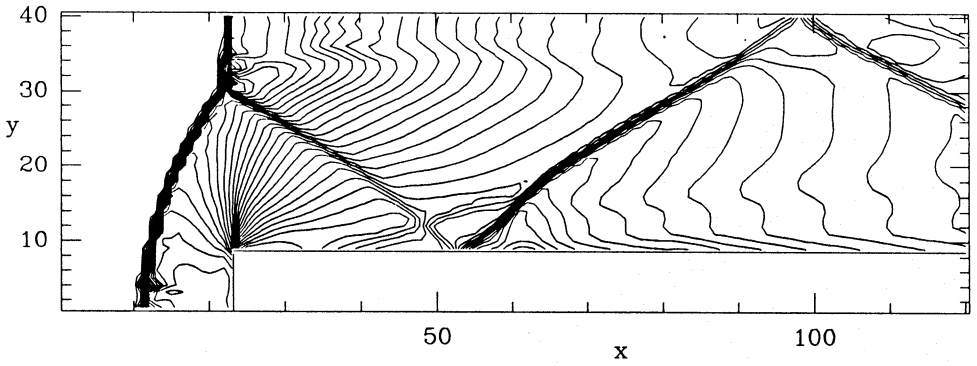

Fig. 8. The windtunnel with step problem. This figure shows a contour plot of the mass density at t=4.0. There are 30 contours linearly spaced between minimum and maximum. The labelling on both axes refers to the grid points, each grid cell is 1/40 length unit

$$
\begin{aligned}
b_1 &= \frac{\gamma-1}{2s^2}\left(\frac{1}{2}[V_r^2+r^2V_\theta^2]\Delta_1 - V_r\Delta_2 - r^2V_\theta\Delta_3 + \Delta_4\right) \\
&\quad - \frac{\gamma-1}{2s}(\Delta_2 - V_r\Delta_1) \\
b_2 &= \frac{\gamma-1}{2s^2}\left(\frac{1}{2}[V_r^2+r^2V_\theta^2]\Delta_1 - V_r\Delta_2 - r^2V_\theta\Delta_3 + \Delta_4\right) \\
&\quad + \frac{\gamma-1}{2s}(\Delta_2 - V_r\Delta_1) \\
b_3 &= \frac{\gamma-1}{s^2}\left([H - V_r^2 - r^2V_\theta^2]\Delta_1 + V_r\Delta_2 + r^2V_\theta\Delta_3 - \Delta_4\right) \\
b_4 &= \Delta_3 - V_\theta\Delta_1.
\end{aligned}
\tag{A5}
$$

For the polar direction the values for the characteristic speeds are given by

$$
\begin{aligned}
\lambda_1 &= V_\theta - s/r \\
\lambda_2 &= V_\theta + s/r \\
\lambda_3 &= V_\theta \\
\lambda_4 &= V_\theta.
\end{aligned}
\tag{A6}
$$

The eigenvectors are

$$
\begin{aligned}
e_1 &= (1, V_r, V_\theta - s/r, H - srV_\theta) \\
e_2 &= (1, V_r, V_\theta + s/r, H + srV_\theta) \\
e_3 &= (1, V_r, V_\theta, \tfrac{1}{2}(V_r^2 + r^2V_\theta^2)) \\
e_4 &= (0, 1, 0, V_r).
\end{aligned}
\tag{A7}
$$

The projection coefficients of a state difference in the polar direction are

$$
\begin{aligned}
b_1 &= \frac{\gamma-1}{2s^2}\left(\frac{1}{2}[V_r^2+r^2V_\theta^2]\Delta_1 - V_r\Delta_2 - r^2V_\theta\Delta_3 + \Delta_4\right) \\
&\quad - \frac{r(\gamma-1)}{2s}(\Delta_3 - V_\theta\Delta_1) \\
b_2 &= \frac{\gamma-1}{2s^2}\left(\frac{1}{2}[V_r^2+r^2V_\theta^2]\Delta_1 - V_r\Delta_2 - r^2V_\theta\Delta_3 + \Delta_4\right) \\
&\quad + \frac{r(\gamma-1)}{2s}(\Delta_3 - V_\theta\Delta_1) \\
b_3 &= \frac{\gamma-1}{s^2}\left([H - V_r^2 - r^2V_\theta^2]\Delta_1 + V_r\Delta_2 + r^2V_\theta\Delta_3 - \Delta_4\right) \\
b_4 &= \Delta_2 - V_r\Delta_1.
\end{aligned}
\tag{A8}
$$

Appendix B: Windtunnel with step problem

Woodward & Colella (1984) subjected several numerical hydrodynamical methods to a number of test problems to compare their qualities. One of the tests they use is a problem first proposed by Emery (1968) and extensively used by Van Leer (1979). In this problem the supersonic flow over a step is modelled. The configuration consists of a tunnel (1 unit high, 3 units long), with reflecting upper and lower boundaries. Supersonic gas ($\mathcal{M} = 3$) is constantly fed in on the left hand side (upstream of the step), and we allow free outflow on the right hand side. At 0.2 units from the left hand side, a 0.1 unit high step is placed. This configuration gives rise to a bow shock in front of the step, which reflects at the top of the tunnel, again at the upper surface of the step, and so on. Features to note in this configuration are the position and length of the Mach stem at the first reflection, the contact discontinuity leaving this stem, and the weak discontinuity leaving the edge of the step, interacting with the reflecting shocks. See Woodward & Colella (1984) for a more thorough overview of the features of this problem.

To compare the behaviour of the Roe solver to that of other codes, we subjected it to this test. The grid we use is a Cartesian one (x, y). This means that the state, fluxes, and sources (Eqs.2.1–2.5) become

$$
\begin{aligned}
W &\equiv (\rho, \rho v_r, \rho v_\theta, e), \\
F &\equiv (\rho v_x, \rho v_x^2 + p, \rho v_x v_y, (e+p)v_x), \\
G &\equiv (\rho v_y, \rho v_x v_y, \rho v_y^2 + p, (e+p)v_y), \\
S &\equiv (0, 0, 0, 0).
\end{aligned}
\tag{B1}
$$

One sees that the source terms are all zero, so the subgrid model (Sec.2.3) amounts to equating the flux at the interface to the flux at the cell centre; the state is assumed constant in a cell.

In Fig.8 we show the result for the Roe solver. It was done on a 120×40 grid, corresponding to the intermediate resolution case in the Woodward and Colella paper. Using their criteria of Mach stem length and position, presence of the Mach stem contact discontinuity over the entire length of the tunnel, and positions of further reflections, our method is comparable to the best codes they tested (MUSCL, PPM). This test shows that the Roe solver method is capable of handling complex two-dimensional shock configurations, and gives confidence in its application to the interacting winds problem.

References

Balick, B., 1987, *Astron. J.* **94**, 671
Balick, B. Preston, H., Icke, V., 1987, *Astron. J.* **94**, 1641
Bedogni, R., D'Ercole, A., 1986, *Astron. Astrophys.* **157**, 101
Blandford R.D., Rees, M.J., 1974, *Monthly Notices Roy. Astron. Soc.* **169**, 395

Boris, J.P., Book, D.L., 1973, *J. Computat. Phys.* **11**, 38
Boris, J.P., Book, D.L., 1976, *J. Computat. Phys.* **20**, 397
Castor, J., McCray, R., Weaver, R., 1975 *Astrophys. J. (Letters)* **200**, L107
Chang, S.-H., and Liou, M.-S., 1988, *NASA Technical Memorandum* 101355
Chevalier, R.A., Imamura, J.N., 1983, *Astrophys. J.* **270**, 554
Emery, R.A., 1968, *J. Computat. Phys.* **2**, 306
Eulderink, F., 1990, in preparation
Frank, A., Balick, B., Riley, J., 1990, *Stellar Wind Paleontology, Shells and Halos of Planetary Nebulae*, preprint
Habing, H.J., te Lintel Hekkert, P., Van der Veen, W.E.C.J., 1989, in: *IAU Symposium 131, Planetary Nebulae*, ed. S. Torres–Peimbert, Reidel, Dordrecht, p. 359
Icke, V., 1988, *Astron. Astrophys.* **202**, 177 (I 88)
Icke, V., 1991, *The Hydrodynamics of Aspherical Planetary Nebulae. I. Analytic Evaluation of Hydrodynamic Difference Schemes, Astron. Astrophys.* in press
Icke, V., Balick, B., Frank, A., 1991, *The Hydrodynamics of Aspherical Planetary Nebulae. II. Numerical Hydrodynamics, First Results*, submitted to *Astron. Astrophys.* (IBF 91)
Icke, V., Preston, H.L., 1989, *Astron. Astrophys.* **211**, 409
Igumenshchev, I.V., Tutukov, A.V., Shustov, B.M., 1989, *Astrophysics* **30**, 168
Kahn, F.D., 1983, in: *IAU Symposium 99, Planetary Nebulae*, ed. D.R. Flower, Reidel, Dordrecht, p. 305
Kahn, F.D., West, K.A., 1985, *Monthly Notices Roy. Astron. Soc.* **212**, 837
Kwok, S., 1982, *Astrophys. J.* **258**, 280
Kwok, S., Purton, C.R., Fitzgerald, P.M., 1978, *Astrophys. J. (Letters)* **219**, L125
Lamers, H.J.G.L.M., 1983, in: *Diffuse matter in galaxies*, ed. J. Audouze, Reidel, Dordrecht, p. 35
Landau, L.D., Lifshitz, E.M., 1987, in: *Course of Theoretical Physics VI, Fluid Dynamics*, Pergamon Press, Oxford
MacLow, M.–M., McCray, R., and Norman, M.L., 1989, *Astrophys. J.* **337**, 141
Norman, M.L., Winkler, K.H.A., Smarr, L.L., 1983, in: *Astrophysical Jets*, eds. A. Ferrari and A.G. Pacholczyk, Reidel, Dordrecht, p. 227
Okorov, V.A., Shustov, B.M., Tutukov, A.V., Yorke, H.W., 1985, *Astron. Astrophys.* **142**, 441
Perinotto, M., 1989, in: *IAU Symposium 131, Planetary Nebulae*, ed. S. Torres–Peimbert, Reidel, Dordrecht, p. 293
Roe, P.L., 1981, *J. Computat. Phys.* **43**, 357
Roe, P.L., 1985, *Lect. in Appl. Math.* **22**, 163
Roe, P.L., 1986, *Ann. Rev. Fluid Mech.* **18**, 337
Schmidt-Voigt M., Köppen, J., 1987, *Astron. Astrophys.* **174**, 211
Shklovskii, I., 1956, *Astronom. Zhurnal* **33**, 315
Soker, N., Livio, M., 1989, *Astrophys. J.* **339**, 268
Strang, G., 1968, *SIAM J. Num. Analysis* **5**, 506
Van Leer, B., 1979, *J. Computat. Phys.* **32**, 101
Weaver, J., McCray, R., Castor, J., Shapiro, P., Moore, R., 1977, *Astrophys. J.* **218**, 377
Woodward, P., Colella, P., 1984, *J. Computat. Phys.* **54**, 115

This article was processed by the author using Springer-Verlag TEX A&A macro package 1991.